An RF-Powered Temperature Sensor Designed for Biomedical Applications

Gustavo Campos Martins and Fernando Rangel de Sousa

Electrical Engineering Department, Federal University of Santa Catarina, CTC/EEL/GRF, Florianópolis, Brazil,
email:gustavocm@ieee.org

***Abstract*—Continuous patient monitoring enables early detection and treatment of diseases. Small and wireless devices are more comfortable to the patient and simplify the implantation procedure. This paper presents the design and partial testing of an integrated RF-powered temperature sensor suitable for the human body temperature range, from 35 to 42^{o}C. The device was designed using a 130-nm standard CMOS technology and it receives energy from a 900-MHz signal that has power as low as –10 dBm. A calibration method was designed to obtain conversion errors smaller than 0.2^{o}C.**

***Index Terms*—Biomedical Electronics, RF Power Transfer, CMOS.**

I. INTRODUCTION

A general application of biomedical electronic devices is continuous patient monitoring, which can enable early detection of diseases or complications, permitting a more effective treatment. To perform this task in a comfortable manner to the patient, the employed device must be small and wireless. One way to reduce size is to remove the device's battery and use an energy harvesting technique or transfer power from an external source [1]. The latter method permits higher power levels at the device. There are several ways of transmitting power and one way of doing it is through electromagnetic waves, in which the transmitted power levels are mainly limited by tissue damaging [2].

There are several kinds of biomedical-signal sensors, and a simple one that can be readily implemented in CMOS technology is the temperature sensor. It is an important sensor for biomedical applications because temperature is a relevant parameter to diagnose many diseases.

One example of a well-known device that implements power transfer and communication to an external device is the fully-passive RFID tag. In this scheme, illustrated in Fig. 1, the external device, called reader, sends power to the tag and the information is sent back from the tag through the reflected signal modulation [3].

This work presents an RF-powered temperature sensor suitable to measure human body temperature (35 to 42^{o}C), developed in a standard 130-nm CMOS technology and designed and simulated with the Cadence environment. Based on the RFID scheme, power and information are transferred between reader and sensor with a 900-MHz signal. The system architecture is presented in the next section, the design of each block and some simulation results are presented in Sec. III, a full-system simulation is discussed in Sec. IV, partial measurement results are presented in Sec. V and, finally, the work is concluded in the last section.

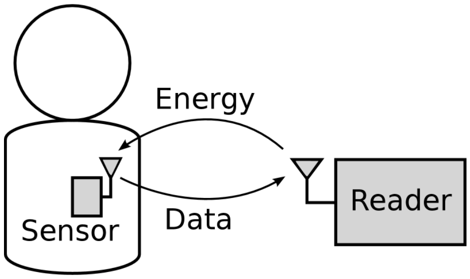

Fig. 1: Diagram of basic power transfer and communication of a basic biomedical sensor

II. SYSTEM ARCHITECTURE

Fig. 2 shows the system block diagram. The RF front end, formed by the impedance matching, rectifier and backscattering device, is responsible for receiving and rectifying the input signal and send information about the measured temperature back to the reader. The remaining blocks do the power management and sense the temperature.

The impedance matching block was designed to provide a 50-Ω input impedance to match our 50-Ω based measurement setup. Next to this block, a rectifier is used to generate a DC supply voltage V_{dc} while charging the C_s capacitor, which is responsible to provide energy autonomy to the system. Since the input signal power can vary, V_{dc} can increase and damage the circuits, so a voltage limiter is employed to limit its value. A mode selector is used to monitor V_{dc} and, based on its value, switch the system between standby and active mode. A voltage regulator is employed to generate the supply voltage V_{dd} of the sensor core. This core is formed by a reference source, which is the most temperature sensitive circuit in the system, and an oscillator. The oscillator is biased with the reference current I_{ref} generated by the source, thus providing a signal with temperature dependent frequency. This signal controls the backscattering device, which modulates the input impedance and, consequently, the reflected signal. Through this reflected signal, the reader device obtains information about the measured temperature.

III. CIRCUIT DETAILS

In this section, the design of each block along with its simulation is presented. The reader device was not imple-

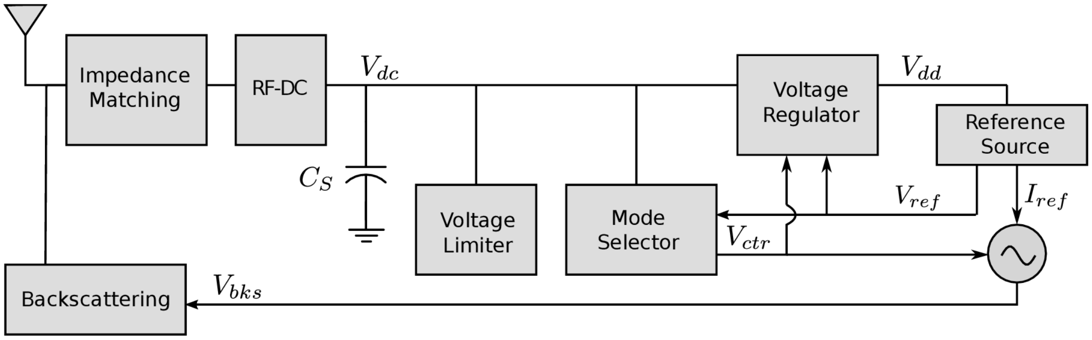

Fig. 2: Block diagram of the sensor device

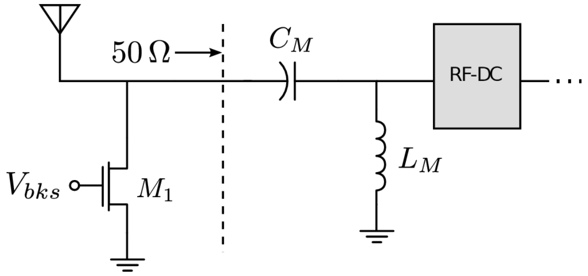

Fig. 3: Schematic of the backscattering device and impedance matching network

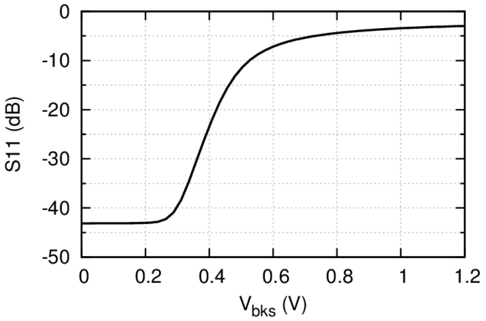

Fig. 4: Backscattering device S11 simulation results control voltage sweep

mented in this work, so we considered the specifications of the reader presented in [4] to design the sensor device.

A. Backscattering Device

The backscattering device is responsible for modulating the input impedance, thus modulating the reflected signal amplitude and phase [3]. This technique is also known as Load Shift Keying (LSK) modulation.

The backscattering device circuit is presented in Fig. 3, along with other elements. It is composed by transistor M1, which works as a switch, ideally commuting the input impedance Z_{in} between 50 and 0 Ω. When Z_{in} = 50 Ω, there is no reflected signal, and when Z_{in} = 0 Ω, the reflected power is at its maximum. This scheme was chosen to increase the maximum distance between reader and sensor, because the reflected signal is the maximum possible.

Transistor M_1 has width W = 50 µm and length L = 120 nm, minimum channel length of the used technology. Fig. 4 shows the S11 simulation results. Considering the reader specifications [4], the Friis transmission equation [5], the losses on the backscattering device and that our system uses a typical RFID antenna of 2 dBi gain [3], the minimum input signal power is approximately −10 dBm and the maximum distance from reader to sensor is 15 m.

B. Rectifier and Impedance Matching

The rectifier topology is presented in Fig. 5 and it is composed of 16 stages that are based on the Greinacher voltage doubler [6]. The transistors in diode configuration are native transistors, enabling the rectifier operation with a lower input signal power. The rectifier was partially designed using the method presented in [7], for an output voltage V_{dc} = 1 V, load current I_{dc} = 10 µA and input power P_{av} = −10 dBm. We obtained 10% of power conversion efficiency (PCE), which is defined by:

$$PCE = \frac{P_{dc}}{P_{av}}, \tag{1}$$

where P_{dc} is the output power and P_{av} is the available power at the input, i.e., the input power if the input impedance is perfectly matched to the source impedance.

The L-match network, composed by L_M and C_M in Fig. 3, was designed to match the input impedance of the rectifier, 219 − 291 jΩ, to 50 Ω. This network was designed considering the parasitics extracted from layout and the chosen values of L_M and C_M were 12 nH and 1.68 pF. With input and output conditions mentioned before, the simulated nominal S11 at 900 MHz is −35 dB. A Monte Carlo simulation with 1000 samples was performed, resulting in a worst case S11 equal of −15 dB.

C. Voltage Limiter

The voltage limiter circuit schematic is presented in Fig. 6 and it is based on the limiter proposed in [8]. This circuit consumes the excess current generated by the rectifier, preventing V_{dc} from increasing to high values. It was designed to limit V_{dc} to 1.6 V, which is the maximum supply voltage permitted by the employed technology.

For V_{dc} increasing, and when V_{dc} is high enough for transistors M_1-M_4 to conduct current, the voltage drop on R_1 increases. When the gate voltage of M_5 is low enough, the current that flows through M_5 increases, thus increasing the

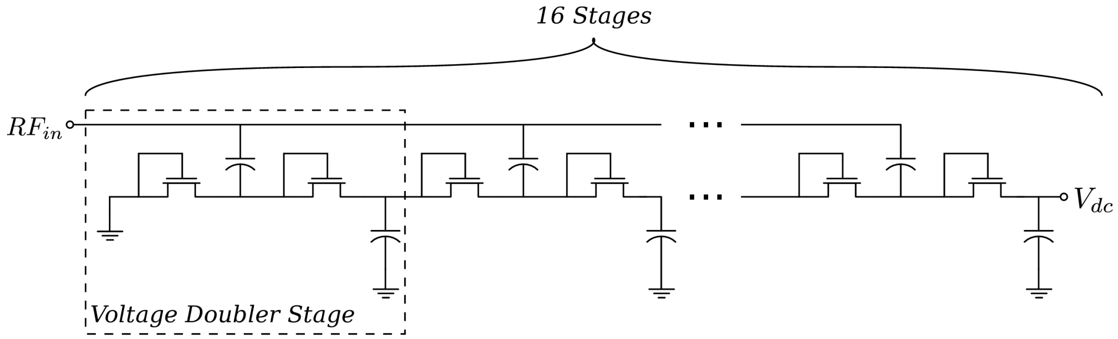

Fig. 5: Rectifier circuit schematics

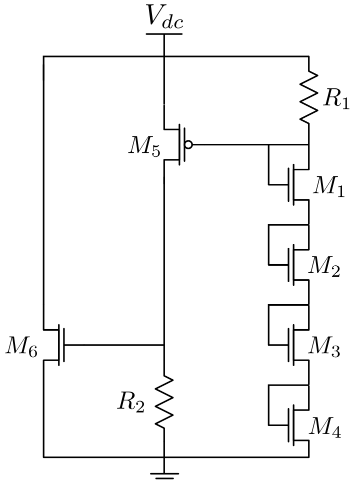

Fig. 6: Voltage limiter schematic

gate voltage of transistor M_6. In this final stage, the current that flows through M_6 is higher than the current of the other branches, limiting the V_{dc} at higher input power levels.

The values of resistors R_1 and R_2 are 20 and 400 kΩ, respectively. The transistor dimensions for all transistors used in this circuit are W = 10 μm and L = 1 μm. Simulation results of the voltage limiter connected to the rectifier (with impedance matching) are presented in Fig. 7. The circuit limits V_{dc} to values not greater than 1.6 V for a wide input power range.

D. Mode Selector

The voltage and current reference source starts up only when its supply voltage V_{dd} is greater than a certain value V_{stable} , i.e., the temperature sensor works correctly only when $V_{dd} > V_{stable}$. So it is interesting to have a block that monitors V_{dc} and turns the sensor on and off at V_{dc} values greater than V_{stable} to not produce an incorrect output. To perform the task, the comparator with internal hysteresis [9] presented in Fig. 8 is employed to compare a reference voltage V_{ref} to a voltage V_{cresc} that increases with V_{dc}. For an increasing V_{dc}, when V_{cresc} is greater than V_{ref} by certain value, the system turns on (starts active mode) at $V_{dc} = V_{on}$. After the system is in active mode and V_{dc} is decreasing, when V_{cresc} is lower than V_{ref} by certain value, the system turns off, which happens at $V_{dc} = V_{off}$. When the system is in active mode, the mode selector output V_{ctr} is high (follows V_{dc}), otherwise (standby mode) V_{ctr} is low. This behavior is shown in Fig. 9 along with the input voltages curves.

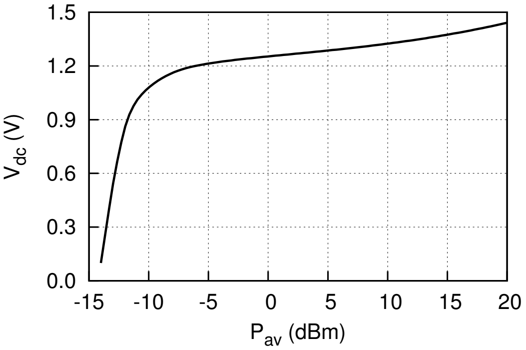

Fig. 7: Voltage limiter simulation results for an input power sweep

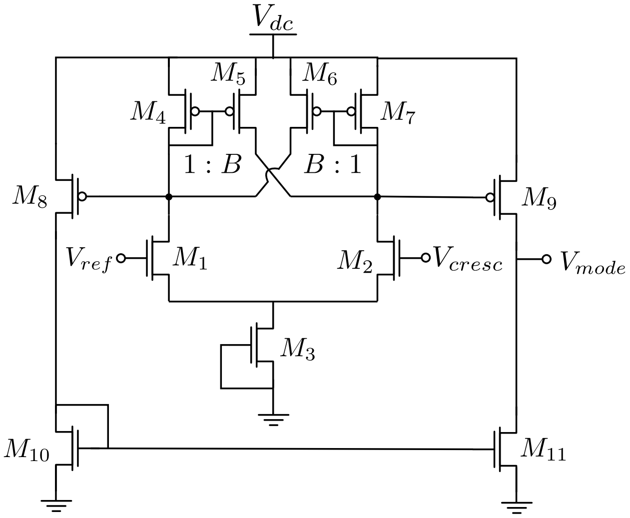

Fig. 8: Mode selector schematic

Transistor M_3 is biased in sub-threshold region, providing a low bias current for the comparator. The transistors dimensions used in this circuit are shown in table 1. The value of the current mirror ratio B, which controls the comparator hysteresis, is 15. We chose B to set the values of V_{on} and V_{off} to 1.05 and 0.75 V, respectively. A Monte Carlo simulation was also performed and, among 1000 samples, not a single sample presented V_{off} lower than V_{stable}, which is 0.6 V, as can be seen in Fig. 9(a). The current consumption of this circuit is 34 nA at V_{dc} = 1 V.

The increasing voltage V_{cresc} generator circuit is presented in Fig. 10. To relate V_{cresc} to V_{ref}, the inputs V_{b0} and V_{b1} come from the reference source in order to mirror its cur-

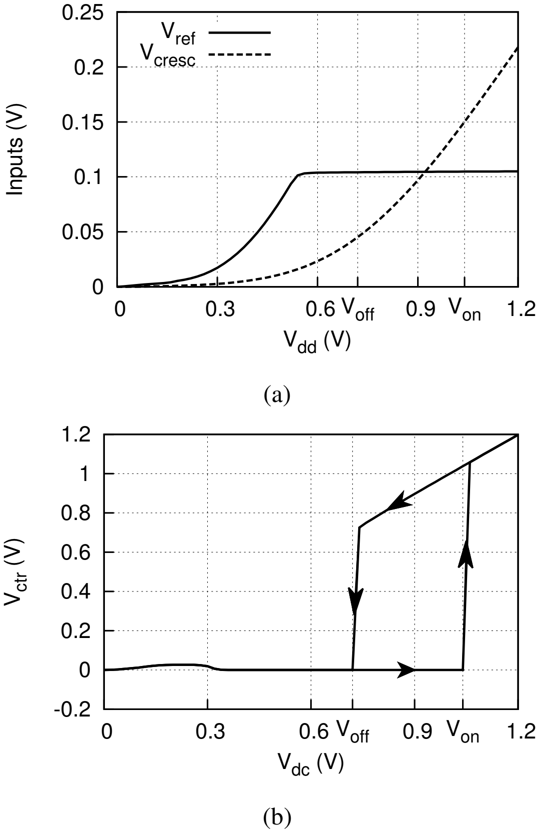

(a)

(b)

Fig. 9: Mode selector simulated (a) inputs and (b) output for V_{dc} increasing and decreasing, direction indicated by the arrows

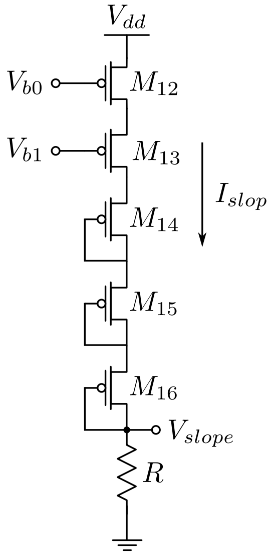

Fig. 10: Increasing voltage generator circuit

rent. The transistors M_{14} -M_{16} are connected as diodes to prevent current from flowing through R at the beginning and keeping V_{cresc} initially lower than V_{ref}. This circuit's transistors dimensions are shown in table 1. The resistance of R is 512 kΩ.

E. Voltage Regulator

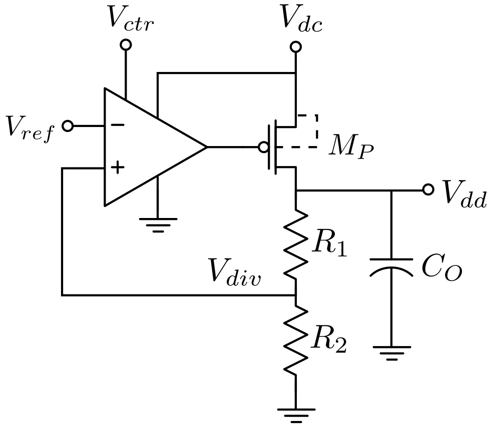

Fig. 11: LDO voltage regulator topology

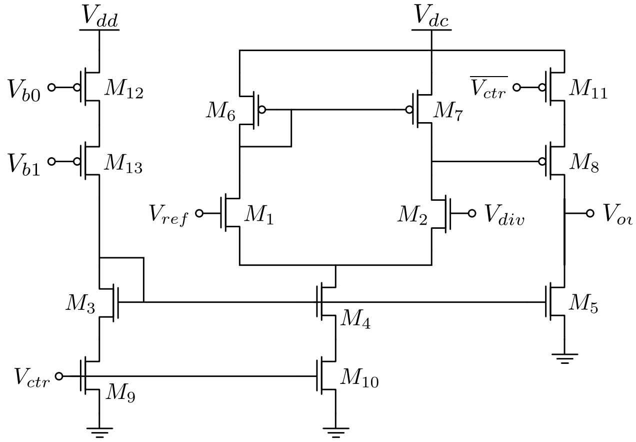

Fig. 12: Operational amplifier circuit used in the LDO regulator

Table 1: Mode selector and increasing voltage generator's transistors dimensions

Transistor	W (µm)	L (µm)
M_1, M_2, M_8, M_9	120	0.42
M_3	80	0.5
M_4, M_7	1	5
M_5, M_6	15	5
M_{10}, M_{11}	2	0.5
M_{12}, M_{13}	18	1.2
M_{14}, M_{16}	8	5

A voltage regulator is necessary to suppress the wide V_{dc} swings influence on the sensor output. We chose to use the Low Dropout (LDO) regulator topology shown in Fig. 11 due to its low voltage drop from the input V_{dc} to the output V_{dd} [10]. The regulator is switched on/off by the mode selector. Since the reference voltage V_{ref} is obtained from the reference source, powered by the regulator output, it is important that V_{dd} follows V_{dc} when the regulator is off to correctly initialize the reference source.

The operational amplifier employed in the regulator is presented in Fig. 12 and it is switched on/off by V_{ctr}. When it is off (V_{ctr} is low), its output voltage is low and current flows through transistor M_P. When V_{ctr} is high, the circuit works as an amplifier. This amplifier does not have internal compensation and the regulator is stable due to its feedback network and load capacitor C_O. The regulator total power consumption is 2.6 µW when turned on. The transistor parameters used in this circuit are presented in table 2. The

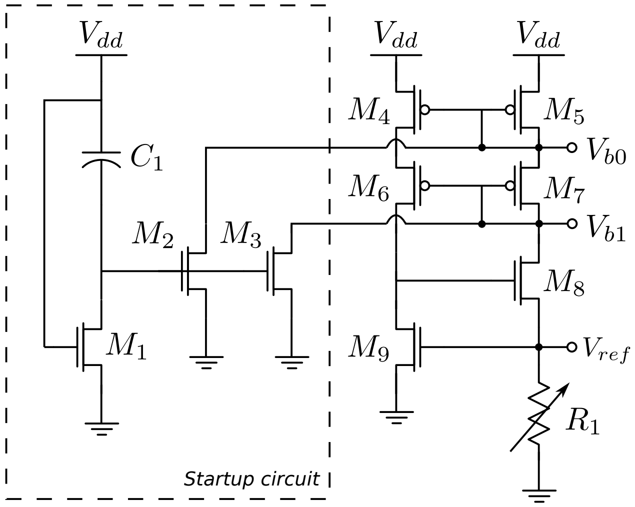

Fig. 13: Threshold-referenced current source

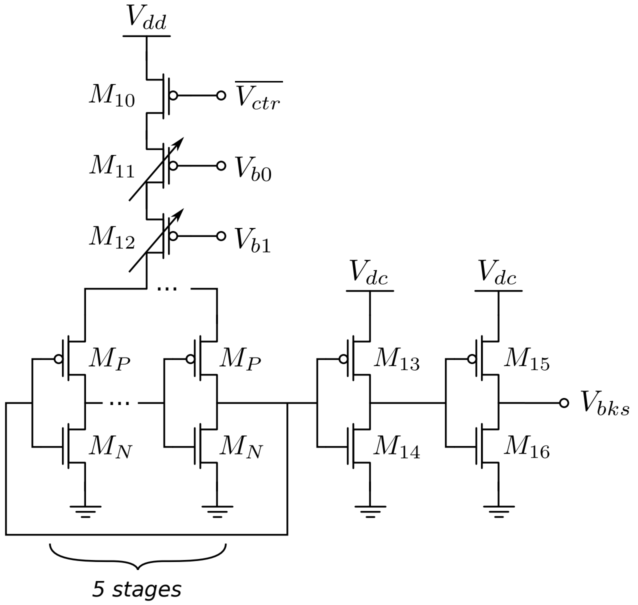

Fig. 14: Current-starved ring oscillator with level shifter

capacitor C_O has 50 pF and the resistors R_1 and R_2 have 3 and 0.5 MΩ, respectively.

F. Temperature Sensor

The threshold-referenced current source presented in Fig. 13 [11] is the most temperature-sensitive circuit in the system and it biases the current-starved ring oscillator, presented in Fig. 14. These two blocks form a temperature sensor which output is a signal that has temperature-dependent frequency.

The reference source nominal current and voltage outputs with respect to temperature and supply variations are presented in Fig. 15. The reference current temperature coefficient is $TC_I = -1.22$ %/°C and its value at T = 38.5°C (middle of the temperature range) is 613 nA. The source starts working with $V_{dd} = V_{stable} = 0.6$ V.

At 38.5°C, the oscillator frequency is 660 kHz and its temperature coefficient is –0.78 %/°C. The transistor M_{10} switches the oscillator on or off. Transistors M_{13}-M_{16} increase the output peak-to-peak voltage to V_{dc}, allowing a greater power reflection of the backscattering device when V_{bks} is high.

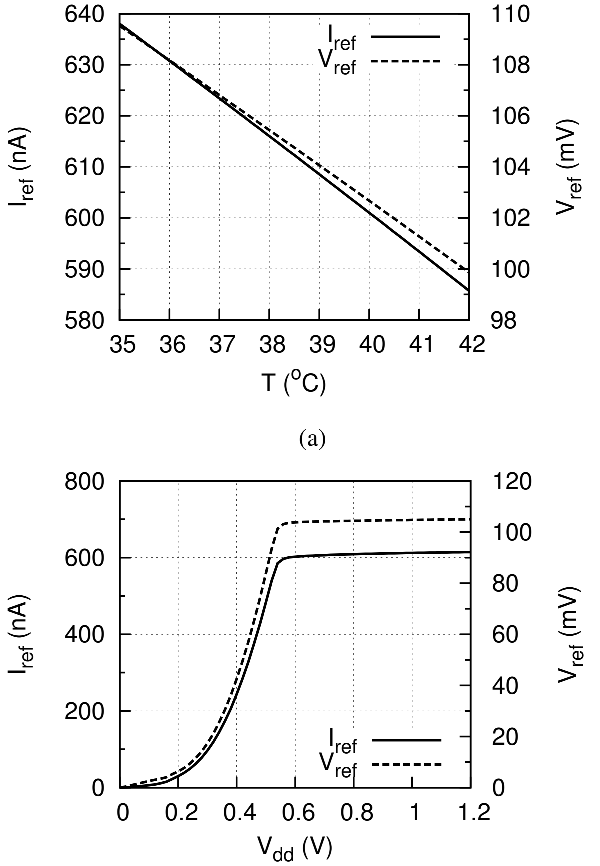

(a)

Fig. 15: Reference source outputs for (a) temperature and (b) supply voltage variations

Table 2: Parameters of components used in the LDO regulator

Transistor	W (μm)	L (μm)
M_1, M_2	15	0.8
M_3, M_4, M_5	3	1.2
M_6, M_7	0.16	3
M_8	0.32	3
M_9, M_{10}	6	1.2
M_{11}	2	0.5
M_{12}, M_{13}	16	1.2
M_P	4	0.5

The transistor dimensions used in the oscillator and reference source are presented in table 3. The capacitor C_1 used in the startup circuit has 1 pF capacitance and the resistors R_1 and R_2 have nominal values of 270 and 512 kΩ, respectively. The power consumption of these two circuits combined is 2.8 μW.

I.Calibration

Due to fabrication process variations, the sensor output will change. To match the output frequency versus tempera-

Table 3: Dimensions of transistors used in the reference source and the oscillator

Transistor	W (μm)	L (μm)
M_1- M_3	0.5	0.5
M_4-M_9, M_{11}-M_{12}, M_{17}-M_{18}	18	1.2
M_{10}	0.5	0.12
M_{13}	1	0.12
M_{14}	2	0.12
M_{15}	1.5	0.12
M_{16}	0.5	0.12
M_{19}-M_{21}	8	5
M_P	3	12
M_N	1	12

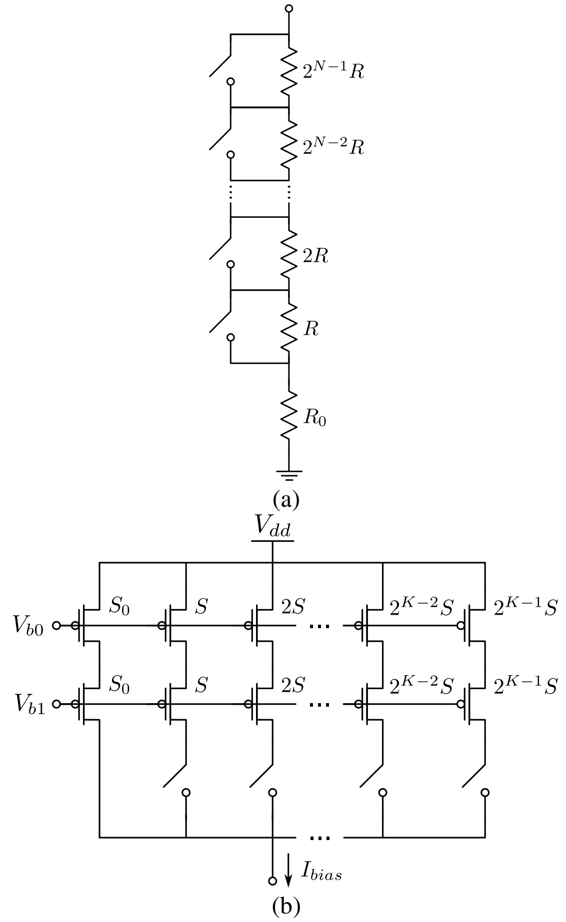

Fig. 16: Variable (a) resistor and (b) current mirror used to calibrate the sensor

ture curve to the nominal one, we designed a two-stage calibration method.

The first stage consists in calibrating the TC through the variation of resistor R_1, since TC_I can be approximated by [11]:

$$TC_I = \frac{1}{V_{t9}}\frac{\partial V_{t9}}{\partial T} - \frac{1}{R_1}\frac{\partial R_1}{\partial T} = TC_{V_{t9}} - TC_{R_I}. \qquad (2)$$

The second stage consists in calibrating the absolute value of the frequency at T = 38.5°C through the variation of transistors M_{11}-M_{12} aspect ratios, i.e., a modification of the current mirror ratio. Ideally, this stage does not modify TC_I and the resulting I_{bias} curve will be fitted to the nominal one. The calibration of I_{bias} current calibrates the output frequency, because the frequency is approximately proportional to the bias current [12].

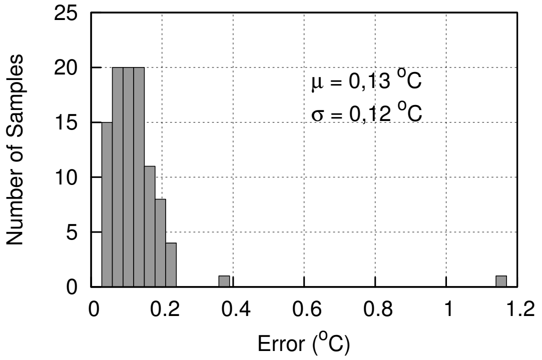

Fig. 17: Conversion error after calibration

The variable resistor is composed by 8 series resistors, of which 7 can be short circuited through switches, as shown in Fig. 16(a). Each variable transistor is composed by 13 shunt transistors as shown in Fig. 16(b), forming current mirrors. These shunt mirrors can be activated by the series switches, modifying the ratio of the equivalent current mirror. The R and R_0 values are 4 and 50 KΩ, respectively, and the aspect ratio S and S_0 values are 7 x 10^{-4} and 0.3, respectively.

We did a 100-sample Monte Carlo simulation with extracted parasitics and calibrated each sample. Due to time limitations, these simulations were performed considering only the reference current. The results are presented in Fig. 17. A total of 96 % of the samples presented less than 0.2°C of conversion error.

IV. FULL-SYSTEM SIMULATION

We did full-system transient simulations with extracted parasitics from layout. The results are presented in Figs. 18 and 19.

The waveforms of the oscillator output V_{bks}, the rectifier output V_{dc} and the voltage regulator output V_{dd} are presented in Fig. 18. These waveforms were obtained at T = 38.5°C and with an input-signal source that had 900-MHz frequency and 50-Ω impedance. After a startup time of 35 μs, the oscillator produces a 627.3 kHz signal. The ripple of V_{dc} after 35 μs is due to the backscattering device operation, i.e., there is a V_{dc} drop because the input power is reflected when V_{bks} is high.

Fig. 19 presents the frequency of V_{bks} in simulations at different temperatures and with several input power levels. Due to time limitations, in these simulations the rectifier with impedance matching was modeled as an ideal current source. For $P_{av} > -9.2$ dBm, the frequency variations produce negligible conversion errors.

V. MEASUREMENTS RESULTS

Some of the circuits described in this paper were sent to fabrication and tested. In this section, the measurement results are presented.

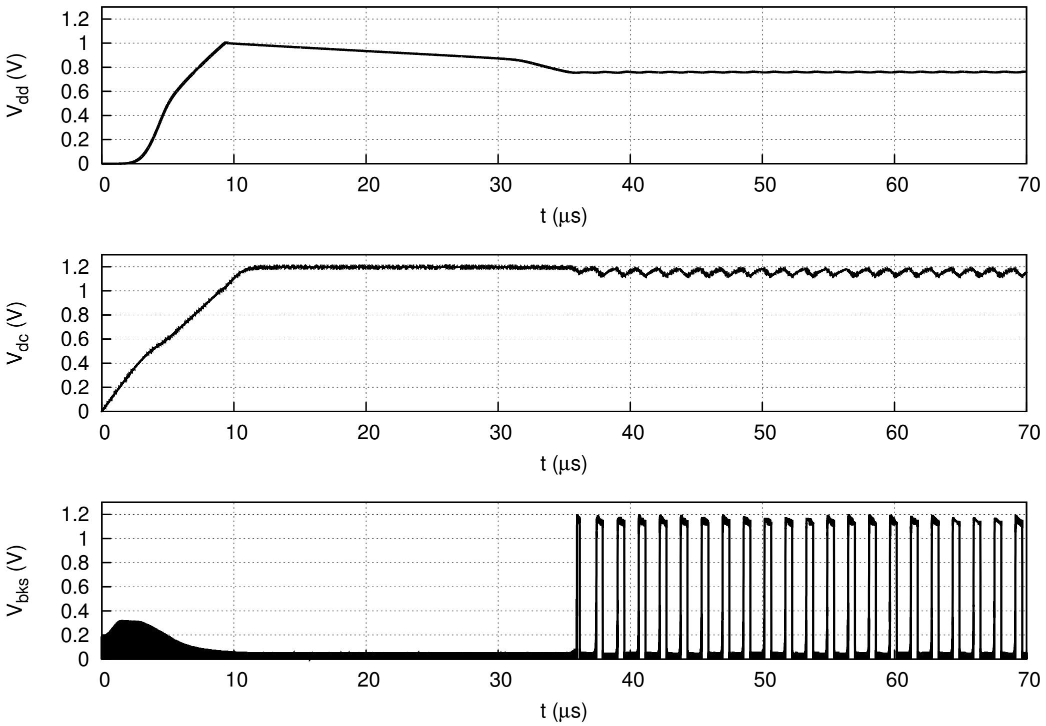

Fig. 18: Transient simulation results

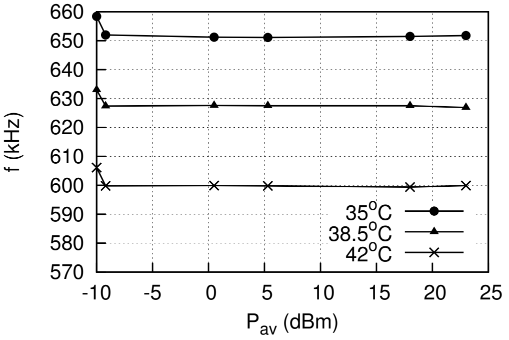

Fig. 19: V_{bks} frequency variation with temperature and input power

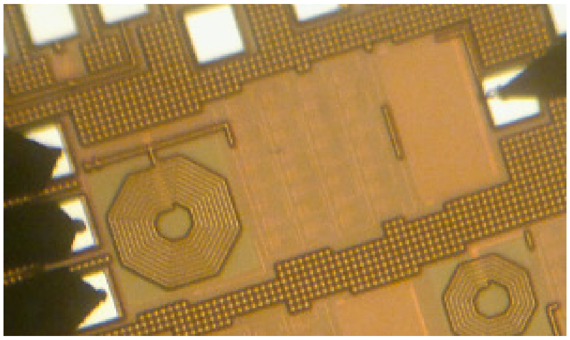

Fig. 20: Photograph of the rectifier with impedance matching and output capacitor during measurements

A. Rectifier

The rectifier with impedance matching circuit and the C_S capacitor are presented in Fig. 20. The RF input probe is on the left side of the photograph and the DC output probe is on the right side.

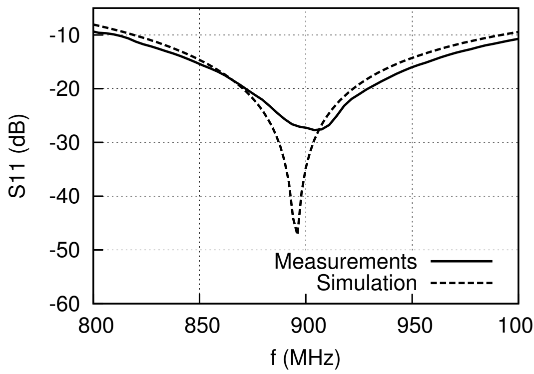

Fig. 21: S11 measurements and simulation results of the rectifier with impedance matching

A 100-kΩ resistor is placed at the rectifier output to act as a 10 µA load current at 1 V output voltage. As expected, the rectifier's PCE is approximately 10% at −10 dBm input signal power. In Fig. 21, the measured S11 is presented. At 900 MHz, we measured S11 equal to −27.4 dB. There is a difference between the S11 obtained through measurements and nominal simulation, although this difference is inside the limits predicted by the Monte Carlo simulation.

B. Voltage Limiter

The measurement results for the voltage limiter circuit are presented in Figs. 22(a) and 22(b) in linear and logarithmic scales, respectively. The results are close to the simulated and at V_{DD} = 1 V the current consumption is 2 µA.

C. Backscattering Device

To test the backscattering device separately from the

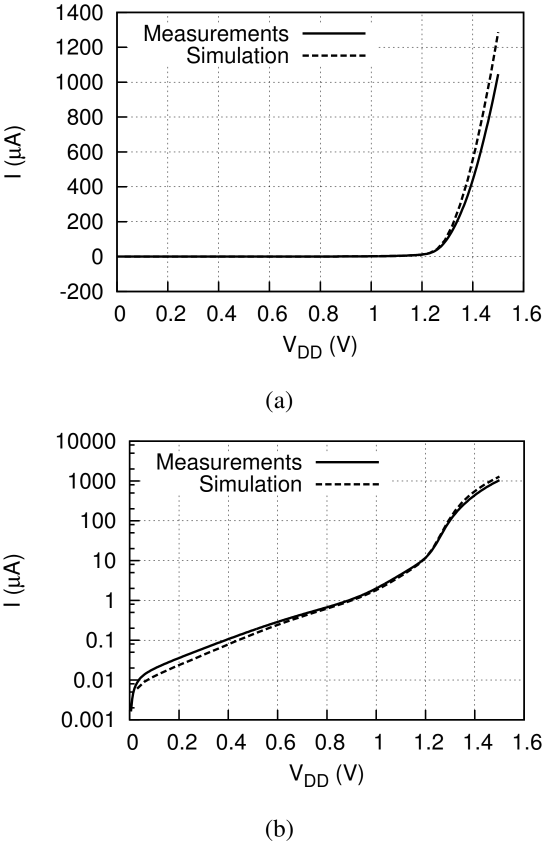

(a)

(b)

Fig. 22: Measurement and simulation results of the voltage limiter in (a) linear scale and (b) log scale

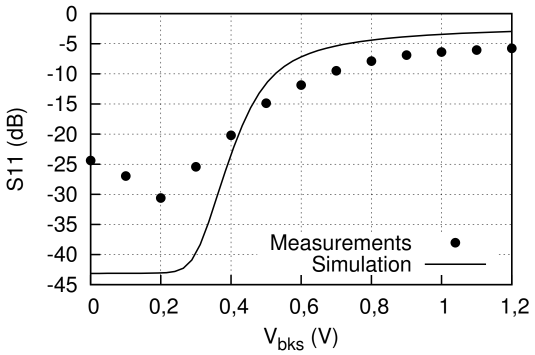

Fig. 23: Measured and simulated S11 of the backscattering device in parallel with a 50 Ω resistor

other circuits, we placed a 50-Ω on-chip resistor in parallel to it. Fig. 23 presents the S11 curve for a sweep of the control voltage V_{bks}. The measured S11 when V_{bks} = 0 V is −24.4 dB, which is far from simulated due to device variability, but is acceptable for defining the matched state. When V_{bks} = 1.2 V the measured S11 is −5.8 dB, which is the unmatched state.

VI. CONCLUSION

The design and partial testing of an integrated RF-powered temperature sensor was discussed. The developed system operates in two modes: standby, in which the system consumes 4.9 µA, and active, in which the current consumption is 8.5 µA. With the minimum input signal specification, the rectifier works with 10% efficiency, providing 10 µA output current. The active area of the combined layouts of all blocks is approximately 0.34 mm^2. The largest layout is the rectifier block one (0.26 mm^2), which includes an inductor (from the impedance matching circuit) and the storage capacitor. The sensor has a temperature coefficient of −0.78 %/°C and maximum conversion error, after calibration, of 0.2°C.

In table 4 we compare our work to recent RF-powered temperature sensors, developed with similar technology and input signal frequency. We managed to develop a system that occupies a small area, if compared to the others, while also containing circuits for sensor calibration.

REFERENCES

[1] R. Vullers, R. Schaijk, H. Visser, J. Penders, and C. Hoof, "Energy harvesting for autonomous wireless sensor networks", IEEE Solid-State Circuits Magazine, 2, pp. 29 –38. 2010.

[2] IEEE, *C95.1-2005 - IEEE standard for safety levels with respect to human exposure to radio frequency electromagnetic fields, 3 khz to 300 ghz.* 2006.

[3] K. Finkenzeller, *RFID handbook: fundamentals and applications in contactless smart cards, radio frequency identification and near-field communication,* Wiley, 2010.

[4] I. Mayordomo, R. Berenguer, A. Garcia-Alonso, A., Fernandez, and I. Gutierrez. "Design and implementation of a long-range rfid reader for passive transponders". *IEEE Transactions on Microwave Theory and Techniques*, pp. 1283–1290, 2009.

[5] H. T. Friis, "A note on a simple transmission formula", *Proceedings of IRE, pp. 254–256*, 1946.

[6] H. Greinacher, "Uber eine methode, wechselstrom mittels elektrischer ventile und kondensatoren in hochgespannten gleichstrom umzuwandeln", *Zeitschrift fur Physik*, pp. 195–205, 1921.

[7] J. A. Cardoso, *Modelagem e projeto de conversores AC/DC de ultrabaixa tensão de operação*. Ph.D. thesis, Universidade Federal de Santa Catarina, 2012.

[8] U. Kaiser and W. Steinhagen, "A low-power transponder ic for high-performance identification systems", *IEEE Journal of Solid-State Circuits, pp. 306–310 ,* 1995.

[9] P. E. Allen and D. R. Holberg, *CMOS analog circuit design,* Oxford Univ. Press, 2002.

[10] J. Wilas, K. Jirasereeamornkul, P. Kumhom, "Power harvester design for semi-passive UHF RFID tag using a tunable impedance transformation", *IEEE Journal of Solid-State Circuits*, pp. 1441-1445, 2009.

[11] P. R. Gray, P. J. Hurst, R. G. Meyer, and S. H. Lewis, *Analysis and design of analog integrated circuits*, John Wiley & Sons, 2008.

[12] K. Sundaresan, P. E. Allen, and F. Ayazi, "Process and temperature compensation in a 7-MHz CMOS clock oscillator", *IEEE Journal of Solid-State Circuits*, pp. 433–442, 2006.

[13] F. Kocer and M. Flynn, 2006. "An RF-powered, wireless CMOS temperature sensor", *IEEE Sensors Journal*, p. 557 –564, 2006.

[14] D. Yeager, F. Zhang, A. Zarrasvand, N. George, T. Daniel, B. Otis, "A 9 µA, Addressable Gen2 Sensor Tag for Biosignal Acquisition", *IEEE Journal of Solid-State Circuits*, pp. 2198 –2209, 2010.

[15] H. Reinisch, M. Wiessflecker, S. Gruber, H. Unterassinger, G. Hofer, M. Klamminger, W. Pribyl, and G. Holweg, "A multifrequency passive sensing tag with on-chip temperature sensor and off-chip sensor interface using EPC HF and UHF RFID technology", *IEEE Journal of Solid-State Circuits*, pp. 3075–3088, 2011.

Table 4: Comparison with recent publications

Reference	[13]	[14]	[15]	[16]	[17]	This Work
Technology (nm)	250	130	130	130	180	130
Input Frequency (MHz)	450	900	900	868	910	900
Area (mm2)	1.2	-	0.95	3.96	1.2	0.34
Standby power consumption (μW)	5	6	-	≈ 0.11	-	4.9
Active power consumption (μW)	1500	9	7.9	-	7	8.5
RF-DC efficiency (%)	-	30*	8.6	35*	-	10
Minimum input power (dBm)	-12.5	-12	-10.3	-	-5	-10

[16] A. Vaz, A. Ubarretxena, I. Zalbide, D. Pardo, H. Solar, A. Garcia-Alonso, and R. Berenguer, "Full passive UHF tag with a temperature sensor suitable for human body temperature monitoring". *IEEE Transactions on Circuits and Systems II: Express Briefs*, pp. 95 –99. 2010.

[17] J. Qian, C. Zhang, L. Wu, X. Zhao, D. Wei, Z. Jiang, and Y. He, "A passive UHF tag for RFID-based train axle temperature measurement system", *Custom Integrated Circuits Conference (CICC)*, 2011.